An investigation of uranium $M_{4,5}$ edge magnetic X-ray circular dichroism in US

# An investigation of uranium $M_{4,5}$ edge magnetic x-ray circular dichroism in US

S P Collins, D Laundy, C C Tang and G van der Laan

Synchrotron Radiation Department, CCLRC Daresbury Laboratory, Warrington WA4 4AD, UK

**Abstract.** Magnetic x-ray circular dichroism (MXCD) has been measured in a ferromagnetic uranium monosulphide crystal by monitoring the fluorescence signal over the uranium $M_{4,5}$ edges. Despite sizeable absorption corrections, we have obtained a precise value of the dichroic branching ratio, which is compared with sum-rule predictions. We find that, in contrast to the case of cubic 3d transition metals where the magnetic dipole term $\langle T_z \rangle$ can be neglected, its contribution to the dichroism signal in the present case is larger than that of the spin polarization, $\langle S_z \rangle$. The dichroism spectrum is shown to exhibit considerably more structure than those of resonant magnetic diffraction from antiferromagnetic actinide compounds, and is found to be in good qualitative agreement with atomic calculations of $5f^2$ and $5f^3$ configurations.

## 1. Background: magnetic scattering and absorption

Interest in magnetic dichroism at uranium M edges stems largely from measurements of resonant magnetic x-ray diffraction (or resonance exchange scattering) from antiferromagnetic actinide compounds. Since the discovery of huge increases in magnetic diffraction intensities from uranium arsenide, at photon energies close to the $M_{4,5}$ absorption edges [1], a wide range of magnetic actinides has been studied by x-ray diffraction [2–5] with magnetic intensities reaching as high as one per cent of the chemical Bragg reflections— a figure closer to the norm for neutrons than x-rays. These unusually large 'resonant enhancements' have been attributed [6] to strong electric dipole transitions from the $3d_{3/2,5/2}$ core levels, to the highly polarized 5f shell, which is largely responsible for the magnetism of actinide ions.

However, scattering and absorption are fundamentally related through the optical theorem [7, 8], which states that the total beam attenuation is proportional to the imaginary (phase-shifted) component of the scattering amplitude in the *forward* direction. One can consider resonant magnetic diffraction as being *caused* by magnetization-dependent attenuation, and therefore strong magnetic sensitivity in scattering should be mirrored in absorption measurements.

The resonant photon scattering amplitude (or scattering length, to correctly describe its dimensional properties), in $SO_2$ (cylindrical) symmetry and in the limit of a weak crystal field, can be written within the dipole approximation [6, 8] as

$$f_r(E) = -\left(\frac{3}{4\pi q}\right)\left\{(\varepsilon'^* \cdot \varepsilon)[F^1_{+1}(E) + F^1_{-1}(E)] + i(\varepsilon'^* \times \varepsilon) \cdot m[F^1_{-1}(E) - F^1_{+1}(E)]\right.$$
$$\left. + (\varepsilon'^* \cdot m)(\varepsilon \cdot m)[2F^1_0(E) - F^1_{+1}(E) - F^1_{-1}(E)]\right\} \tag{1}$$

in terms of which the scattering cross-section is simply

$$\frac{d\sigma}{d\Omega} = |f_r|^2. \tag{2}$$

Here, $\varepsilon$, $\varepsilon'$ are the primary and secondary (scattered) beam polarization unit vectors, $q = 2\pi/\lambda$ is the photon wave vector magnitude and $F_\nu^1(E)$ are dimensionless energy-dependent dipole transition strengths [8] with magnetic components $\nu = 0, \pm1$.

For weak forward scattering the photon polarization state is preserved; we have $\varepsilon = \varepsilon'$, and the polarization cross-product in (1) vanishes unless the polarization vectors are complex, which we identify with a state of circular polarization. It is, perhaps, useful to comment that after averaging over all possible magnetic directions (i.e. spherical symmetry) the forward scattering limit of (1) reduces to $f_r(E) = -(1/2\pi q)[F_{+1}^1(E)+F_{-1}^1(E)+F_0^1(E)]$, which is known as the isotropic spectrum. A form of (1) where the transition probability has been separated specifically into isotropic and dichroism spectra can be found for instance in [9, 10]. For experimental geometries where the symmetry vector and photon beam are collinear, the third term in (1) vanishes, leaving no sensitivity to $F_0^1(E)$. This is, in fact, the present case, so we keep only the first two terms of scattering length.

The total linear attenuation coefficient can be derived from (1), by making use of the optical theorem [11]

$$\begin{aligned}
\gamma(E) &= \left(\frac{4\pi n_0}{q}\right) \operatorname{Im} f_r(E, k = 0) \\
&= -\left(\frac{3n_0}{q^2}\right) \operatorname{Im}\left\{(\varepsilon^* \cdot \varepsilon)[F_{+1}^1(E)+F_{-1}^1(E)]+i(\varepsilon^* \times \varepsilon)\cdot m[F_{-1}^1(E) - F_{+1}^1(E)]\right\} \\
&= -\left(\frac{3n_0}{q^2}\right)\left\{\operatorname{Im}[F_{+1}^1(E) + F_{-1}^1(E)] - P_2\hat{q} \cdot m \operatorname{Im}[F_{-1}^1(E) - F_{+1}^1(E)]\right\} \tag{3}
\end{aligned}$$

where $P_2$ is the Stokes parameter for circular polarization (i.e. the average helicity), and $n_0$ represents the density of atoms in the target.

The first term in (3) is the average attenuation, which is independent of the photon circular polarization state and becomes the isotropic absorption spectrum when linear dichroism is negligible, i.e. where $2F_0^1(E) \simeq F_{+1}^1(E) + F_{-1}^1(E)$. The second term, known as magnetic x-ray circular dichroism (MXCD), couples the photon circular polarization $P_2$ to the projection of the target's magnetic vector $m$ along the photon propagation vector, $q$. The precise contribution that MXCD makes to the total attenuation coefficient $\gamma(E)$ can be determined experimentally, by reversing the target magnetization $m$ (or $P_2$), thereby reversing the sign of the dichroism term. The difference in attenuation coefficients for the two configurations,

$$\Delta\gamma = 2\left(\frac{3n_0}{q^2}\right) P_2\hat{q} \cdot m \operatorname{Im}[F_{-1}^1(E) - F_{+1}^1(E)] \tag{4}$$

is the magnetic dichroism signal, which depends on precisely the same difference in resonance strengths as magnetic diffraction.

Data from resonant magnetic x-ray diffraction experiments and MXCD are therefore very closely related, but differ in two key aspects. Firstly, dichroism is sensitive only to the *imaginary* part of the resonant amplitude, and secondly, as a 'bulk' probe, MXCD provides no *spatial selectivity and can be applied only to materials with a net magnetic polarization*. While diffraction (and, in fact, *linear* dichroism [12]) can provide spectroscopic data on antiferromagnets, circular dichroism requires ferri- or ferromagnetic targets.

## 2. Measurements on uranium monosulphide

Without doubt, the simplest and most reliable method of obtaining accurate absorption data is by measuring the attenuation of an x-ray beam through a uniform thin foil. Unfortunately, this is not always practical. Even when thin foils or films of a suitable thickness (typically submicrometre for soft x-ray photons) are available, they are commonly either polycrystalline or amorphous. Since most magnetic actinide compounds exhibit considerable magnetocrystalline anisotropy, one would clearly prefer to perform dichroism measurements on single-crystal samples.

There are, however, a number of indirect techniques for determining absorption spectra with thick targets, of which two have found particular prominence. The first relies on the detection of Auger and associated secondary electrons, emitted in radiationless transitions which de-excite the atomic core-hole states generated by photon absorption. In the second approach, secondary (fluorescence) x-ray photons from radiative de-excitation modes are monitored. Both methods are backed by arguments suggesting a proportional relationship between the intensity of secondary radiation and the absorption cross-section [13, 14]. We have adopted the latter method, which does not require the high-vacuum conditions required for electron yield detection.

A convenient target for these measurements is a crystal which can be magnetized by a compact conventional electromagnet, has a large 5f magnetic moment, and can be cooled below the Curie temperature, $T_C$, by a nitrogen gas cryostat system. (The latter requirement is to allow a cold crystal to fit within the 6 mm pole gap of our 1 T electromagnet.) Uranium monosulphide ($T_C \simeq 177$ K, $\mu_{uranium} \simeq 1.7$ $\mu_B$), was deemed to be ideal, with a modest (<1 T) field directed along a ⟨111⟩ easy axis of the cubic NaCl crystal structure sufficient to achieve a high degree of magnetic saturation.

Average $M_{4,5}$ absorption spectra can be inferred from measurements of the total fluorescence intensity as a function of the primary photon beam energy. In this case, a Ge (111) channel-cut monochromator provided a nominal energy bandwidth of 1.3 eV (smaller than the 4 eV core-hole lifetime width), and the fluorescence signal was monitored by a germanium solid state detector (figure 1). Placing the detector as close as possible (~2.5 cm) to the target crystal ensured a large solid angle of detectable photons. Working at photon energies of 3.5–3.8 keV, serious loss of signal intensity can arise from absorption in air; a distance of just 8 cm can attenuate the primary or secondary beam by more than a factor of two. To alleviate this problem, most air paths were replaced by helium-filled tubes, sealed with 6 $\mu$m Kapton windows. The lower curve of figure 4 is an example of such a total fluorescence spectrum.

Observation of MXCD requires the photon helicity to be alternately parallel and antiparallel to the target magnetization. The difference in fluorescence intensity between the two configurations reveals the dichroic signal. A number of techniques are available for generating circularly polarized synchrotron radiation. Special insertion devices based, for example, on elliptical or crossed undulators [15, 16] promise very high fluxes of polarized photons, while alternative methods, such as the x-ray quarter-wave phase plate, have already proved highly effective in dichroism studies [17]. Our approach is much simpler.

Synchrotron radiation emitted by dipole bending magnets becomes increasingly circular in polarization at progressively larger angles above or below the beam centre [18, 19]. While a corresponding loss in flux bars the use of beams with *complete* circular polarization, one can readily extract partially polarized radiation with small intensity losses. For the present measurements, extracting the beam at ±0.10 mrad provided a calculated circular polarization of $P_2 \simeq 0.52$ with nearly 90% of the peak flux (in fact, the choice of viewing angle, and
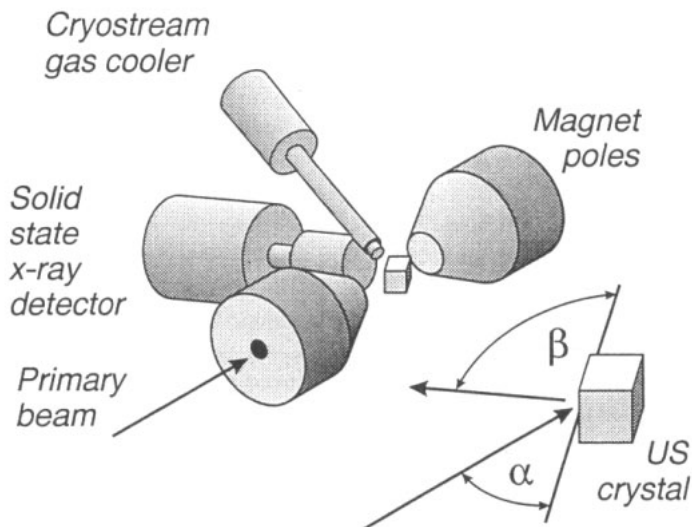
**Figure 1.** The experimental layout for uranium M-edge magnetic circular dichroism measurements by fluorescence detection. The primary and secondary (fluorescence) x-ray beams subtend the illuminated crystal face at angles $\alpha = 35°$ and $\beta = 55°$, respectively.

hence circular polarization, was restricted by the fixed monochromator crystal height).

Having obtained a suitable source of circularly polarized photons, dichroism measurements proceeded by observing the *fractional* change in fluorescence rate, $\Delta I / I = (I_+ - I_-)/(I_+ + I_-)$, upon switching between opposite $(+, -)$ magnetic field directions in a 2 s asynchronous cycle. Figures 2 and 3 display the variation in dichroic asymmetry near the $M_4$ peak, with magnetic field strength and temperature, respectively. Combined with the observation of the anticipated sign change on reversal of the photon helicity (by extracting radiation from above and below the beam centre), the graphs confirm the signal to be magnetic in origin, and the small electromagnet to be adequate to saturate the sample magnetization along an easy axis.
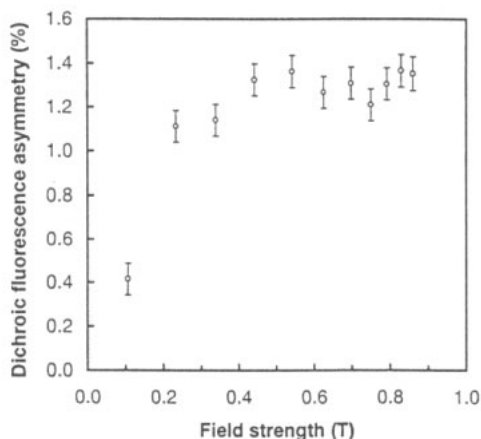


**Figure 2.** The dichroic asymmetry, $\Delta I / I = (I_+ - I_-)/(I_+ + I_-)$, near the uranium $M_4$ peak, as a function of applied field with the target crystal at 100 K.
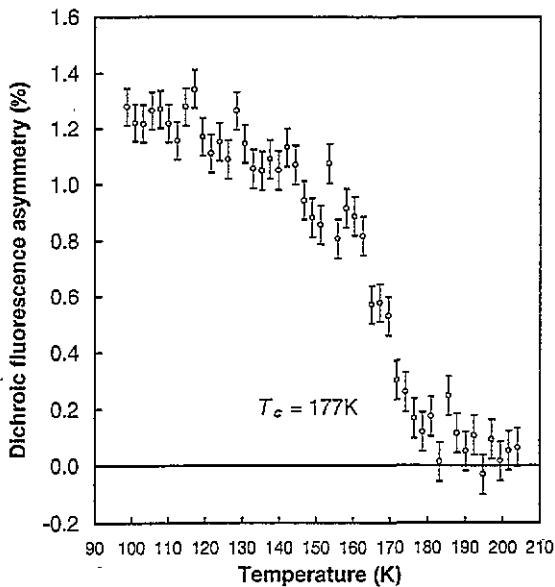
**Figure 3.** The M$_4$ dichroic asymmetry versus crystal temperature with an applied field of 0.83 T. Note that the signal drops rapidly near the Curie temperature of 177 K.

All subsequent measurements of the dichroic *spectrum* (figures 4 and 5) were performed with a field of ±0.83 T and the temperature kept at 100 K. While the total fluorescence in figure 4 is visibly distorted by very strong sample absorption variations, the asymmetry, generated by circular dichroism, clearly exhibits considerable structure. The M$_4$ peak is quite symmetric, and has the same sign as the much weaker M$_5$ peak. This is precisely what was inferred from magnetic diffraction measurements [1]. The M$_5$ magnetic resonance is highly asymmetric, and between the two peaks oscillations reminiscent of extended x-ray absorption fine structure (EXAFS) are observed. Some preliminary results on US are given in [20].

## 3. Data analysis

In order to obtain the dichroism spectrum, $\Delta\gamma(E)$, from the fluorescence asymmetry, $\Delta I/I$ in figure 4, three steps are required. First, one must correct the data for photon absorption variations, converting fluorescence intensities to attenuation coefficients. Second, the dichroism data have to be corrected for the finite circular polarization, $P_2$, of the primary beam. Finally, one must multiply the relative dichroism, $\Delta\gamma(E)/\gamma(E)$, by the total attenuation, $\gamma(E)$, to reveal the absolute dichroism signal. The combined effect of these operations produces a dichroism spectrum (figure 5) in which the strong features (the M$_{4,5}$ white lines) become more pronounced with respect to weaker structures, and narrow considerably in width.

We now consider the data corrections in more detail, turning first to the absorption correction, which has two distinct origins. The simplest of these arises from the energy-dependent attenuation of the primary and secondary photon beams by materials other than the target crystal. This contribution, mainly due to air, beryllium and the germanium dead layer of the x-ray detector, exhibits a simple energy dependence. It does *not* affect the relative dichroism. The second (and typically the largest) absorption correction does
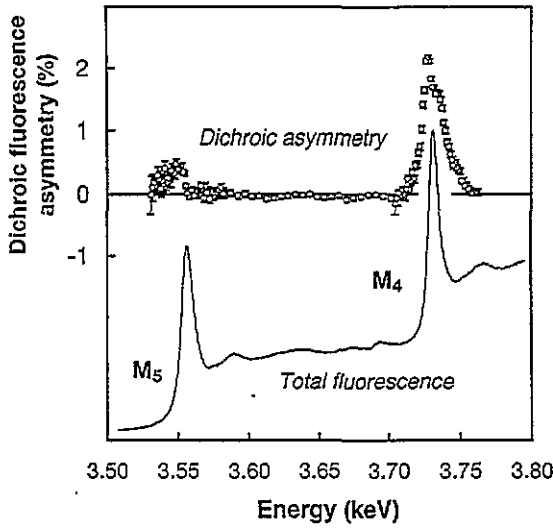
**Figure 4.** The measured total fluorescence spectrum, $I(E)$ (lower curve), and dichroic asymmetry, $\Delta I/I$ (upper curve). Note that severe absorption variations tend to scale down the strong resonances in both the total and magnetic spectra, broaden the peaks, and reduce the intensities at the low-energy end of the spectrum.
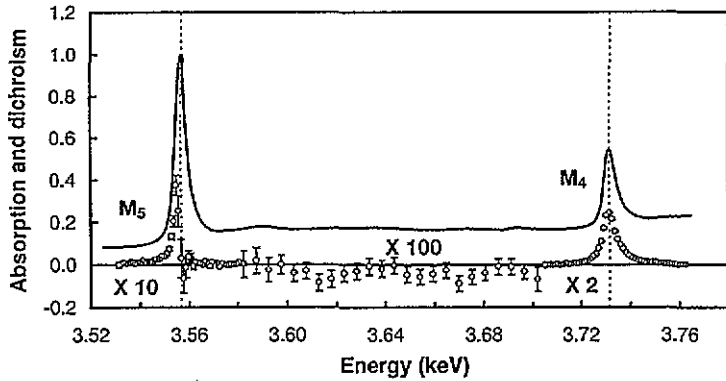


**Figure 5.** The absorption spectrum, $\gamma(E) = \gamma_+ + \gamma_-$ (solid line) and dichroism $\Delta\gamma(E) = \gamma_+ - \gamma_-$ (error bars), both normalized to unity at the peak of $\gamma(E)$. The data have been corrected for absorption and the dichroism spectrum normalized to $P_2 = +1$. The absorption corrections are quite severe, approaching a factor of five at the $M_5$ edge.

alter the relative dichroism. It arises from attenuation variations within the target crystal, which lead to strongly energy-dependent photon penetration depths, and a scaling down, or saturation, of the strongest resonant features.

The appropriate absorption correction to map the fluorescence rate, $I_{M_{4,5}}$ on to the corresponding linear attenuation coefficient, $\gamma_{M_{4,5}}$, with the geometry illustrated in figure 1 is

$$\gamma_{M_{4,5}}(E) = \frac{\gamma_0(E)/\sin\alpha + \gamma(E'_{M_{4,5}})/\sin\beta}{A/I_{M_{4,5}}(E)\exp\left((-\gamma t_{in}(E) - \gamma t_{out}(E'_{M_{4,5}})\right) - 1/\sin\alpha} \tag{5}$$

with a correction for the relative dichroism spectrum of

$$\left(\frac{\Delta\gamma_M}{\gamma_M}\right) = \frac{(\Delta I_M/I_M)}{1 - \left(\gamma_M/(\gamma_M + \gamma_0 + \gamma(E'_{M_{4,5}})\sin\alpha/\sin\beta)\right)}. \tag{6}$$

The symbols in the above expressions are defined as follows: $\gamma_M = \gamma_{M_4}(E) + \gamma_{M_5}(E)$, uranium M edge attenuation coefficients; $\gamma_0(E)$, non-M edge US attenuation coefficient; $\gamma t_{in}(E) = \gamma_{air}(E)t_{air} + \gamma_{Be}(E)t_{Be}$, attenuation of primary beam *before* sample; $\gamma t_{out}(E'_{M_{4,5}}) = \gamma_{air}(E'_{M_{4,5}})t_{air} + \gamma_{Be}(E'_{M_{4,5}})t_{Be} + \gamma_{Ge}(E'_{M_{4,5}})t_{Ge}$, attenuation of fluorescence radiation *after* sample; $\gamma(E'_{M_{4,5}})$, sample attenuation of fluorescence; $I_M = I_{M_4}(E) + I_{M_5}(E)$, fluorescence rates from $M_{4,5}$ excitations; $A$, adjustable parameter.

We have assumed that the $M_4$ and $M_5$ fluorescence spectra each exhibit a single transition, namely the $M_4N_6$ and $M_5N_7$ lines at $E' = 3.17$ and 3.38 keV, which actually account for around 90% of the total intensity [21]. Not doing so would add even more complexity to the already cumbersome expressions in (5) and (6).

The attenuation coefficients required in (5) and (6) are slowly varying functions of photon energy, $E$, and have been extracted from power-law fits to atomic calculations [22]. Similarly, a comparison between calculated and measured coefficients at a single energy can yield the parameter $A$. However, in the present case the absorption corrections are so large, and sensitivity to the input parameters so great, that we have employed two further scale factors: one for the beryllium, germanium and air attenuation, and a second for the fluorescence absorption within the target crystal. By adjusting these parameters, the total uranium attenuation coefficients were forced to exhibit an $M_4$ peak to edge jump ratio of $\simeq 6.5$, matching the results of previous absorption measurements [23], and an $M_5$ to $M_4$ intensity ratio of 2.1, determined from the atomic calculations described later in this paper. The extra scale factors were both close to two, with no additional scaling required to describe the relative dichroism spectrum.

The question of the net circular polarization in the monochromatic primary beam is also far from trivial. Prior to the double-bounce monochromator crystal, we calculate a value of $P_2 = \pm 0.52$ for beams extracted at $\pm 0.10$ mrad. With very small monochromator diffraction angles (i.e. high-energy, low-order reflections) the monochromator induces a modest departure from the circular polarization of the unconditioned synchrotron beam. However, as the scattering angle approaches $2\theta = 90°$, the linear polarization component *within* the scattering plane (the $\pi$ state) is reduced dramatically with respect to the orthogonal $\sigma$ component. In dynamical diffraction, calculation of the monochromatic beam circular polarization, $P'_2$, is a complex problem. Essentially, three factors are important [24]. First, the $\sigma$ and $\pi$ Darwin widths differ by a factor of $\cos 2\theta$, reducing the $\pi$ intensity more than the $\sigma$. Second, there is a phase shift between the two orthogonal linear components which further reduces the circular polarization. Finally, the peak reflectivity for the $\pi$ state is reduced since the longer extinction depth leads to increased absorption.

We have employed a simple model for the circular polarization which neglects absorption changes, but takes into account two Darwin widths and a simple description of the phase shift. Briefly, we assume that the reflectivity curves are 'top hat' functions, with widths which differ by a factor of $\cos 2\theta$, and that the phase of each linear polarization state varies linearly from $-\pi/4$ to $+\pi/4$ across the reflectivity curve. Within this model, a symmetric $(+ - + - \ldots)$ crystal arrangement tends to produce a large reduction in polarization on the first reflection, due to a combination of the double Darwin width and phase shift. Subsequent reflections reduce the polarization by a smaller amount, since only the accumulated phase shift plays a role. (In fact, with an even number of reflections in an asymmetric (e.g. $+ - - +$) arrangement the phase shift cancels, as outlined in [25].)

While this model is simplistic, it does have the advantage that one can write an analytical expression for the monochromatic beam circular polarization

$$P_2' = \frac{2P_2 \cos 2\theta (\sin R)/R}{P_3(1 - \cos 2\theta) + (1 + \cos 2\theta)} \qquad R = \frac{N\pi}{4}(1 - \cos 2\theta) \qquad (7)$$

where $P_3$, $P_2$ and $P_2'$ are the Stokes parameters for linear polarization of the polychromatic beam, and circular polarization of the polychromatic and monochromatic beams, respectively. The number of (symmetric) crystal reflections is given by $N$, and for the present measurements we have $N = 2$. For uranium $M_{4,5}$-edge studies with a Ge (111) monochromator, we have $2\theta \simeq 61$–$65°$, and the circular polarization is approximately halved to $P_2'(M_4) \simeq 0.24$ and $P_2'(M_5) \simeq 0.21$.

For comparison, we can also write the polarization for the *opposite* extreme, where absorption is much stronger than scattering. This is simply the weak-scattering limit. One can adopt a number of techniques to determine the photon polarization following an $N$-bounce crystal monochromator (for example, the compact density matrix approach described in [8]), leading to the result

$$P_2' = \frac{2P_2 \cos^N 2\theta}{(1 + P_3) + (1 - P_3)\cos^{2N} 2\theta}. \qquad (8)$$

The weak-scattering model predicts a reduced circular polarization at the $M_4$ edge of $P_2' = 0.13$. One might therefore expect the polarization from a real crystal to fall somewhere between these two extreme models, giving values for the present experiment which are perhaps slightly lower than those of equation (7). Since the overall uncertainty in the beam polarization is considerably less than that of the absorption correction, though, we feel that the simple model outlined above is perfectly adequate.

## 4. Dichroism and resonant magnetic diffraction

The first thing to notice about the dichroism spectrum in figure 5 is its striking similarity to the magnetic diffraction spectra from a number of antiferromagnetic uranium compounds (see, for example, [1]). This is, of course, no accident as the two processes are linked through the optical theorem (equation (3)). The $M_4$ to $M_5$ peak ratio in diffraction (after performing an absorption correction very similar to the present one) is around two decades, compared to one decade for dichroism. This is expected, since the former scales with the *square* of the magnetic scattering length. Moreover, the destructive interference observed between the $M_{4,5}$ peaks in diffraction indicates that the magnetic resonances are of the same sign, confirmed by the present results and electron yield measurements on $USb_{0.5}Te_{0.5}$ and $UFe_2$ powders [26]. (Note that, in spin magnets such as 3d metals, spin–orbit-split magnetic resonances are always of opposite sign, reflecting the opposite spin–orbit coupling of the core states. Resonances of the *same* sign indicate a significant orbital polarization of the magnetic ground state.)

Looking in more detail at the diffraction and dichroism spectra, both exhibit approximately symmetric $M_4$ peaks, in stark contrast to the highly asymmetric $M_5$ resonances. Here, the similarities end. The $M_5$ line-shape in diffraction is dominated by spectacular interference effects between the broad *real* tails of the two strong resonances. The structure is well described by a simple Lorentzian resonance at each edge

$$[F_{-1}^1(E) - F_{+1}^1(E)] = \frac{a_{M_4}}{(E - E_{M_4}) + i(\Gamma/2)} + \frac{a_{M_5}}{(E - E_{M_5}) + i(\Gamma/2)} \qquad (9)$$

where $E_{M_{4,5}}$ are binding energies for single magnetic resonances of amplitude $a_{M_{4,5}}$, and $\Gamma$ is the core-hole lifetime width. The successful application of such a simple, structureless model reveals that there is very little sensitivity to the underlying magnetic spectrum. In contrast, absorption spectroscopy is only sensitive to the narrower *imaginary* components of the scattering length (see equation (4)). Lifetime broadening is far less pronounced, and the $M_5$ lineshape cannot be modelled by a single Lorentzian. The measured structure in MXCD is of fundamental importance and not merely an artifact of the experiment. Similarly, the very weak, relatively broad, EXAFS-like features observed between the $M_4$ and $M_5$ resonances in figure 5 are absent in the diffraction spectra. Again, the broad real resonant tails of the strong resonances dominate the spectrum far from the resonant centres, obscuring more subtle features.

While a survey of the literature [27–31] confirms that dichroism data consistently exhibit more spectroscopic structure than resonant diffraction from a wide range of magnetic materials, the latter remain important for two key reasons. First, magnetic diffraction can provide very accurate values of the *integrated* resonance signals at various absorption edges. Second, and most importantly, the spatial sensitivity of diffraction can play a crucial role, not least in enabling measurements to be performed on antiferromagnets.

## 5. Integrated dichroism signals and the sum rules for local moments

In this section, we compare our findings for the integrated $M_{4,5}$ dichroism signals with various moments by applying the appropriate sum rules. First, we adopt the naive assumption that the magnetic dipole term $\langle T_z \rangle$ is negligible, and show that this leads to very poor agreement with Hund's rule ground-state values. After establishing that $\langle T_z \rangle$ is large, we introduce the effective spin moment $\langle S_e \rangle$, which includes the magnetic dipole term, and demonstrate a qualitative accord with Hund's rule predictions for the ratios of the moments. Furthermore, by combining our results with those of a neutron diffraction measurement, we provide a unique value of $\langle T_z \rangle$. Finally, we show that the present results for $\langle S_e \rangle / \langle L_z \rangle$ and $\langle T_z \rangle$ agree well with atomic calculations of U $5f^2$ and $5f^3$ configurations in the intermediate coupling scheme.

Following the derivation of sum rules [32, 33, 34] relating the integrated dichroism signal over pairs of spin–orbit-split core-level excitations to the ground-state spin and orbital projections, $\langle S_z \rangle$ and $\langle L_z \rangle$, several authors have employed x-ray absorption spectroscopy to obtain values for spin and orbital magnetic moments [33, 35]. Since it is experimentally difficult to determine the isotropic spectrum, which requires a complete averaging over all magnetization directions, we have made the assumption $[F_{+1}^1(E) + F_{-1}^1(E) + F_0^1(E)] \simeq 3/2[F_{+1}^1(E) + F_{-1}^1(E)]$, which is equivalent to saying that magnetic linear dichroism, governed by $[2F_0^1(E) - F_{+1}^1(E) - F_{-1}^1(E)]$, is weak. For the present case, this assumption is justified by computing the linear dichroism for a uranium $5f^2$ configuration using Cowan's code [37]. Even with a fully aligned moment, we find that the correction to the above approximation is smaller than 3%, which is well within the error bars of the experimentally derived moments. Moreover, there is no effect on the ratios of moments.

The first sum rule relates the measured integral ratio

$$\rho = \frac{\int_{M_4+M_5} \Delta\gamma(E)\,dE}{\frac{3}{2}\int_{M_4+M_5} \gamma(E)\,dE} \tag{10}$$

to the net ground-state orbital polarization, via the expression

$$\rho = \frac{1}{2}\frac{l(l+1)+2-c(c+1)}{l(l+1)\,n_h}\langle L_z \rangle \tag{11}$$

where $c$ and $l$ are, respectively, the orbital momenta of the core level and the localized valence state, and $n_h = 4l + 2 - n$ is the number of valence holes in the ground state. For the present example (3d–5f), we have $c = 2$, $l = 3$, and the required expression reduces to

$$\rho = \frac{1}{3\,n_h} \langle L_z \rangle. \tag{12}$$

A second sum rule connects the ratio

$$\delta = \frac{\int_{M_5} \Delta\gamma(E)\,\mathrm{d}E - \left(\frac{c+1}{c}\right) \int_{M_4} \Delta\gamma(E)\,\mathrm{d}E}{\frac{3}{2} \int_{M_4+M_5} \gamma(E)\,\mathrm{d}E} \tag{13}$$

to the net spin polarization, $\langle S_z \rangle$. This rule is more complicated to apply as it is also sensitive to the expectation value of the magnetic dipole operator $\langle T_z \rangle$, which describes *correlations* between the spin and position of each electron. In dealing with cubic 3d transition metals, it has been argued [33] that the contribution from $\langle T_z \rangle$ is negligible compared with $\langle S_z \rangle$. Although there is no obvious justification for making such a claim in the case of uranium $M_{4,5}$ edges, we nonetheless adopt this position as a *starting* point, and write the second sum rule as

$$\delta = \frac{l(l+1) - 2 - c(c+1)}{3c\,n_h} \langle S_z \rangle = \frac{2}{3\,n_h} \langle S_z \rangle. \tag{14}$$

From the measured dichroic integrals, we have

$$\begin{aligned}
\delta &= +0.121 \Rightarrow \langle S_z \rangle = +2.2 \\
\rho &= -0.100 \Rightarrow \langle L_z \rangle = -3.6
\end{aligned} \tag{15}$$

where we have taken $n = 2$, although the choice of $n$ is not too critical as long as $n \ll n_h$.

Some comments on the experimental uncertainties associated with these values are in order. The *statistical* errors in the integrated dichroism signals are rather small; around one per cent for the $M_4$ edge, and ten per cent for the weaker $M_5$ resonance. However, both integrals have been significantly modified by the data corrections outlined in section 3. We estimate that the net uncertainty in the values of $\delta$ and $\rho$, and hence in $\langle S_z \rangle$ and $\langle L_z \rangle$, may be as high as $\pm 30\%$, being dominated by systematic errors in the data corrections. The error in the *ratio* of the $M_5$ to $M_4$ resonance integrals, on the other hand, is quite small, since the corrections applied to the two edges are comparable in magnitude. The small value of the $M_5$ to $M_4$ ratio of $0.13 \pm 0.03$, even with this very cautious error estimate, leads to the remarkably precise result

$$\frac{\delta}{\rho} = -1.21 \pm 0.06 \tag{16}$$

which, within the present model, gives

$$\frac{\langle S_z \rangle}{\langle L_z \rangle} = \frac{1}{2} \frac{\delta}{\rho} = -0.61 \pm 0.03. \tag{17}$$

Unfortunately, the predicted total moment of $M = 2\langle S_z \rangle + \langle L_z \rangle = 0.8\ \mu_B$ does *not* tally with the findings of neutron diffraction, which suggest $M = 1.7\ \mu_B$. Furthermore, the spin to orbital ratio in (17) is at odds with both a magnetic form factor analysis [36] (which gives $\langle S_z \rangle / \langle L_z \rangle = -0.22$) and calculations based on a likely Hund's-rule ground state. The latter can simply be written as

$$\frac{\langle S_z \rangle}{\langle L_z \rangle} = \frac{J(J+1) - L(L+1) + S(S+1)}{J(J+1) + L(L+1) - S(S+1)} \tag{18}$$

which, for a less than half-filled 5f shell reduces to

$$\frac{\langle S_z \rangle}{\langle L_z \rangle} = \frac{-S}{L+1} = \frac{-n^{\cdot}}{n(2l-n+1)+2} \tag{19}$$

and takes on values of $-0.17$, $-0.21$ and $-0.29$ with $l = 3$ and $n = 2$, 3 and 4, respectively. The *orbital* moment, on the other hand, does agree reasonably well with the neutron assignment [36] of $M_L = -3.0\ \mu_B$, so it would appear that the problem lies with our treatment of the second sum rule for the spin. Evidently, neglecting $\langle T_z \rangle$ is *not* valid in the present case.

Our next step is to admit the possibility of a significant contribution from $\langle T_z \rangle$, whence the second sum rule becomes [34]

$$\delta = \frac{l(l+1) - 2 - c(c+1)}{3c\,n_h}$$

$$\times \left( \langle S_z \rangle + \frac{l(l+1)[l(l+1) + 2c(c+1) + 4] - 3(c-1)^2(c+2)^2}{2l(l+1)[l(l+1) - 2 - c(c+1)]} \langle T_z \rangle \right)$$

$$= \frac{2}{3n_h}(\langle S_z \rangle + 3\langle T_z \rangle). \tag{20}$$

For convenience, we will refer to the combination $(\langle S_z \rangle + 3\langle T_z \rangle)$ as the *effective spin*, $\langle S_e \rangle$, and our main experimental result is then $\langle S_e \rangle / \langle L_z \rangle = -0.61 \pm 0.03$. This ratio can again be computed for a Hund's-rule ground-state, by writing [34]

$$\langle T_z \rangle = (l - n + \tfrac{1}{2})$$

$$\times \frac{3(S-J)^2(S+J+1)^2 - L(L+1)[L(L+1) - 2S(S+1) + 2J(J+1)]}{2(2l+3)(2l-1)(2L-1)S(J+1)}. \tag{21}$$

Table 1 gives a list of calculated moments for a number of 5f Hund's-rule configurations. Still, none of the Hund's-rule ground states reproduce the experimental value of $\langle S_e \rangle / \langle L_z \rangle$, but the results are already more in line with the measurements. By combining the values for $\langle S_z \rangle$ and $\langle L_z \rangle$ derived from neutron diffraction with the present results for $\langle S_e \rangle / \langle L_z \rangle$, we can obtain a unique and rather precise estimate for the expectation value of the magnetic dipole operator

$$\langle T_z \rangle = \frac{\langle L_z \rangle}{3} \left( \frac{\langle S_e \rangle}{\langle L_z \rangle} - \frac{\langle S_z \rangle}{\langle L_z \rangle} \right) = 0.39 \pm 0.03 \tag{22}$$

which can be compared with the predictions in table 1. Again, none of the Hund's-rule values are in close agreement with the experimental data.

Table 1. The calculated moments of Hund's-rule ground states. The moments have been rescaled with the same factor to yield the correct (experimental) total moment, $M$. The calculated total moments prior to rescaling are denoted by $M^*$.

| Configuration | $\langle L_z \rangle$ | $\langle S_z \rangle$ | $\langle T_z \rangle$ | $\langle S_e \rangle$ | $\langle S_e \rangle / \langle L_z \rangle$ | $M^*$ $(\mu_B)$ | $M$ $(\mu_B)$ |
|---|---|---|---|---|---|---|---|
| U 5f¹ ¹F₅/₂ | $-2.3$ | 0.29 | 0.46 | 1.7 | $-0.72$ | $-2.1$ | $-1.7$ |
| U 5f² ³H₄ | $-2.6$ | 0.43 | 0.25 | 1.2 | $-0.46$ | $-3.2$ | $-1.7$ |
| U 5f³ ⁴I₉/₂ | $-3.0$ | 0.63 | 0.09 | 0.9 | $-0.31$ | $-3.3$ | $-1.7$ |
| U 5f⁴ ⁵I₄ | $-4.0$ | 1.13 | 0.12 | 1.5 | $-0.38$ | $-2.4$ | $-1.7$ |

The failure of the Hund's-rule model to provide a good quantitative description of experimental data on actinides can be understood by computing the 5fⁿ magnetic ground

states in intermediate coupling. One finds that the strong 5f spin–orbit interaction and the 5f–5f Coulomb interactions (cf. table 2) mix other $LSJ$ levels into the Hund's-rule ground state. This has a particularly strong effect on the quadrupole moment $\langle Q_{zz} \rangle$, on $\langle l \cdot s \rangle$, and therefore also on $\langle T_z \rangle$ (see appendix). Atomic calculations show that for uranium $5f^2$, the purity of the Hund's rule ground state $^3H_4$ is only 65%, with contributions also from $^3F_4$, $^1G_4$, $^3F_3$ and $^3H_5$. The final states of interest are those with a 3d core-level hole and an extra 5f electron, $3d^9 5f^{n+1}$ $(J'M')$, which are accessible from the ground-state $5f^n(JM)$ with the dipole selection rules $\Delta J = 0, \pm 1$ and $\Delta M = 0, \pm 1$. Cowan's atomic Hartree–Fock program with relativistic corrections [37] provided values of the Slater and spin–orbit parameters (tables 2 and 3), which were subsequently reduced by 20% to include the effects of intra-atomic relaxation.

**Table 2.** The *ab initio* Hartree–Fock values (eV) of the Slater and spin–orbit parameters in the initial state configurations.

| Configuration | $F^2(5f, 5f)$ | $F^4(5f, 5f)$ | $F^6(5f, 5f)$ | $\zeta(5f)$ |
|---|---|---|---|---|
| U $5f^2$ | 9.514 | 6.224 | 4.569 | 0.261 |
| U $5f^3$ | 8.857 | 5.748 | 4.204 | 0.235 |

**Table 3.** The *ab initio* Hartree–Fock values (eV) of the Slater and spin–orbit parameters in the final state configurations.

| Config. | $F^2(5f, 5f)$ | $F^4(5f, 5f)$ | $F^6(5f, 5f)$ | $\zeta(5f)$ | $\zeta(4d)$ | $F^2(3d, 5f)$ | $F^4(3d, 5f)$ | $G^1(3d, 5f)$ | $G^3(3d, 5f)$ | $G^5(3d, 5f)$ |
|---|---|---|---|---|---|---|---|---|---|---|
| U $3d^9 5f^3$ | 10.025 | 6.572 | 4.831 | 0.301 | 73.384 | 2.564 | 1.190 | 2.003 | 1.211 | 0.847 |
| U $3d^9 5f^4$ | 9.425 | 6.136 | 4.495 | 0.275 | 73.386 | 2.357 | 1.089 | 1.832 | 1.107 | 0.774 |

The branching ratio for circular dichroism, $I_{M_5}/(I_{M_5} + I_{M_4})$, is equal to 1 and 0.02 for an excited state with a single electron in a 5f level with $j = \frac{7}{2}$ and $j = \frac{5}{2}$, respectively. (In fact, the first of these results is a simple consequence of the dipole selection rules, since a $j = \frac{3}{2}$ to $j = \frac{7}{2}$ transition must involve a change of more than one unit of angular momentum.) This explains qualitatively the low branching ratios of the $5f^{2,3}$ configurations, since for $n \leqslant 6$ all electrons are in the $j = \frac{5}{2}$ level. In intermediate coupling the branching ratio of the circular dichroism increases to 0.052 and 0.16 for $5f^2$ and $5f^3$, respectively.

The results of atomic calculation are given in table 4, where the moments have been renormalized to reproduce the total 5f moment of $M = -1.7$ $\mu_B$. The justification for rescaling the moments in tables 1 and 4 stems from the fact that a *weak* crystal field has no effect on the shape of absorption spectra [38], changing only the overall intensities and moments by a constant factor. This is a rather interesting phenomenon, worthy of further comment. Although the intermediate-coupling ground state is a linear combination of different $LSJ$ levels, a weak crystal field which is much smaller than the $LSJ$ level splitting will preserve this linear combination and therefore the ratios $\langle L_z \rangle : \langle S_z \rangle : \langle T_z \rangle$ of the ground state (provided, of course, that we do not change the spin–orbit or 5f–5f Coulomb interactions). The effect of symmetry breaking due to the crystal field is similar to the case of photoemission, discussed in [39]. For a *small* crystal field the shape of the circular dichroism will not change, hence the branching ratio remains the same. This fixes the ratio of the moments $\langle L_z \rangle : \langle S_z \rangle : \langle T_z \rangle$, since these moments are directly related to the branching ratio by the sum rules. Of course, the total intensity of the dichroism may change, but a

constant spectral shape dictates that the moments $L_z$, $S_z$ and $T_z$ scale together. This is the justification for reducing the total moment $M$, while keeping $\langle S_e \rangle / \langle L_z \rangle$ fixed. This scaling works very well with actinides and rare earths, but tends to break down with 3d transition metals, where the crystal fields are typically as high as 1–2 eV.

**Table 4.** The calculated moments for the $5f^n$ atomic ground state configurations in intermediate coupling. The moments have been rescaled with the same factor to reproduce the known total 5f moment, $M$. The calculated total moments before rescaling are denoted by $M^*$.

| Configuration | $\langle L_z \rangle$ | $\langle S_z \rangle$ | $\langle T_z \rangle$ | $\langle S_e \rangle$ | $\langle S_e \rangle / \langle L_z \rangle$ | $M^*$ ($\mu_B$) | $M$ ($\mu_B$) |
|---|---|---|---|---|---|---|---|
| U $5f^1$ | −2.6 | 0.43 | 0.29 | 1.3 | −0.50 | −1.4 | −1.7 |
| U $5f^2$ | −2.4 | 0.36 | 0.42 | 1.6 | −0.66 | −3.3 | −1.7 |
| U $5f^3$ | −2.8 | 0.55 | 0.31 | 1.5 | −0.53 | −3.4 | −1.7 |
| U $5f^4$ | −3.7 | 0.99 | 0.12 | 1.4 | −0.37 | −2.5 | −1.7 |

Before comparing the atomic calculations with our results for $\langle S_e \rangle / \langle L_z \rangle$ and $\langle T_z \rangle$, we note that the second sum-rule is not exact: it does not account for the influence of the 3d–5f electrostatic interaction, which also transfers spectral weight from the M$_4$ to M$_5$ edge [40]. We can estimate the magnitude of this correction by comparing the M$_4$ and M$_5$ intensities in the calculated dichroism spectrum with the calculated values for the ground-state moments. This gives a correction of 3%, resulting in the revised ratio, $\langle S_e \rangle / \langle L_z \rangle = -0.59 \pm 0.03$, and $\langle T_z \rangle = 0.37 \pm 0.03$.

Returning to table 4, we find that the experimental values of both $\langle S_e \rangle / \langle L_z \rangle$ and $\langle T_z \rangle$ are approximately mid-way between those computed for uranium $5f^2$ and $5f^3$ configurations (this is consistent with a neutron diffraction analysis [41], which favours $5f^2$). We therefore conclude that the ground state is expected to be mainly a mixture of these two configurations with a crystal field. The weight of each configuration in the ground state depends on the precise value of the charge-transfer energy, hybridization and on-site Coulomb interaction.

## 6. Dichroic spectra and line-shapes

In addition to the integrated intensities at the uranium M$_{4,5}$ edges, we can compare the calculated MXCD spectra for $5f^{2,3}$ (figure 6) with the experimental data. Bearing in mind the estimated $\pm 30\%$ uncertainty in the overall scaling of the measured dichroism spectrum, calculated M$_4$ peaks for both the $5f^2$ and $5f^3$ configurations agree in shape and magnitude with our findings. Neither of the calculations predict significant structure of the M$_4$ resonance, and indeed very little was found. In contrast, the M$_5$ calculations exhibit considerable structure, which is very sensitive to the atomic configuration. Qualitatively, this is in accord with our findings, which show the weak M$_5$ peak to be far more structured than M$_4$. The precise shape of the M$_5$ dichroism, however, is not reflected in either calculation but seems to be closer to $5f^2$.

## 7. Conclusions

The main conclusions drawn from the present experimental and theoretical study of uranium M-edge circular dichroism can be summarized as follows.

(1) Fluorescence detection offers a very powerful probe of magnetic dichroism following core-level excitation. This has proved particularly valuable for measurements in the 3–4 keV
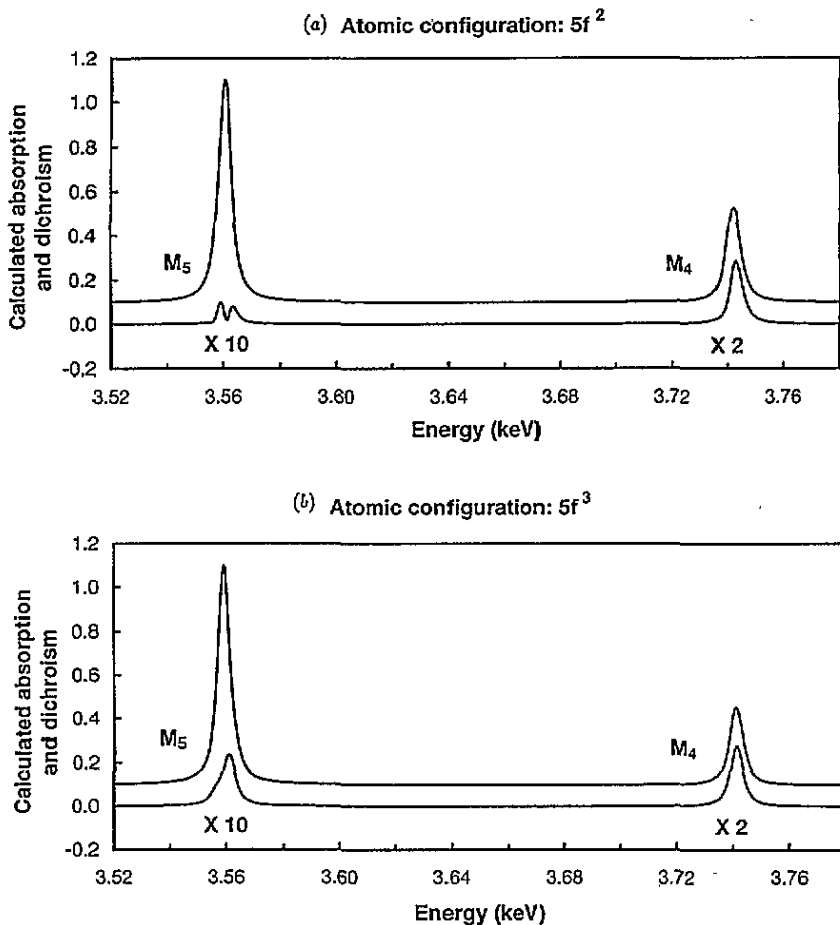
(a)  Atomic configuration: 5f$^2$



(b)  Atomic configuration: 5f$^3$



**Figure 6.** Atomic calculations of the absorption spectrum (normalized to unity and offset for clarity), and circular dichroism, for the 5f$^2$ and 5f$^3$ configurations. The calculated spectra have been convoluted with a Lorentzian of FWHM= 4.0 eV and a Gaussian of FWHM = 1.9 eV, to simulate the effects of lifetime broadening and instrument resolution. The latter was increased from a nominal value of 1.3 eV to match the calculated M$_4$ and M$_5$ widths in the total attenuation to the measured values of 6.3 eV and 5.3 eV, respectively. Note that, to facilitate comparison with figure 5, the M$_{4,5}$ dichroism signals have been multiplied by factors of ten and two.

region, which have confirmed strong MXCD at uranium M edges and Pd L edges [42]. In non-dilute systems, though, the large absorption corrections can add considerably to the experimental errors unless the total absorption spectra are very well characterized.

(2) The results of these measurements agree qualitatively with those of resonant magnetic diffraction from antiferromagnetic uranium compounds [1], but the MXCD spectra exhibit considerably more structure than diffraction. This is largely because the broad real resonant tails which smear out the diffraction spectra are absent in absorption.

(3) The sum rules for integrated intensities in MXCD spectra, which have been applied successfully to the determination of spin and orbital local moments in 3d, 4f and 5d metal ions [33, 35], cannot, in isolation, provide unique values for the spin moment in uranium (5f) ions, since the strong spin–orbit interaction produces a very large value for the magnetic dipole term, $\langle T_z \rangle$.

(4) Integrated MXCD intensities in US are not well described by a Hund's-rule ground state, again due to strong spin–orbit coupling, but are close to the results for $5f^2$ and $5f^3$ atomic configurations in intermediate coupling.

(5) A *quantitative* description of both the integrated intensities and MXCD spectral lineshapes requires an atomic calculation which accounts for hybridization with the valence levels of neighbouring atoms in a crystal lattice.

## Acknowledgments

## Appendix: some notes on the evaluation and interpretation of $\langle T_z \rangle$

It is instructive to calculate the values of the ground-state moments for an $f^1$ configuration [43]. Since $l$ and $s$ are coupled antiparallel for less than half-filled shells, the state vector is a sum over spin orbitals and therefore the moments are frustrated

$$\psi_{j,m_j} = \sum_{m,\sigma} (-1)^{l-s-m_j} (2j+1)^{1/2} \begin{pmatrix} l & s & j \\ m & \sigma & m_j \end{pmatrix} \psi_{l,m} \chi_\sigma. \tag{A1}$$

Inserting $l = 3$, $s = \frac{1}{2}$, $j = l - s = \frac{5}{2}$ and $m_j = -j = \frac{-5}{2}$ in (A1) gives the one-electron wavefunction

$$|\psi\rangle = f^1({}^1F_{5/2,-5/2}) = \sqrt{\tfrac{6}{7}}\,\psi_{3,-3}\chi_{1/2} - \sqrt{\tfrac{1}{7}}\,\psi_{3,-2}\chi_{-1/2}. \tag{A2}$$

Since this wavefunction is normalized to unity, we have

$$n = \langle\psi|\psi\rangle = \tfrac{6}{7} + \tfrac{1}{7} = 1 \tag{A3}$$

for the number of electrons. The total orbital moment is simply

$$\langle L_z \rangle = \langle\psi|l_z|\psi\rangle = -\tfrac{20}{7} \tag{A4}$$

and similarly one can write the spin polarization (i.e. half of the spin moment) as

$$\langle S_z \rangle = \langle\psi|s_z|\psi\rangle = \tfrac{5}{14}. \tag{A5}$$

Likewise, the quadrupole moment is the expectation value of the quadrupole operator, $q_{zz}$

$$\langle Q_{zz} \rangle = \langle\psi|q_{zz}|\psi\rangle = \langle\psi|l_z^2 - \tfrac{1}{3}l(l+1)|\psi\rangle = \tfrac{30}{7}. \tag{A6}$$

$\langle Q_{zz} \rangle$ measures the alignment of the orbital with the magnetic moment by spin–orbit interaction. The anisotropy of the electronic charge induced by the crystalline field of the lattice is relatively small with f metals, and can be neglected in the first instance. A sum rule relates the quadrupole moment to linear dichroism [38]

$$\langle Q_{zz} \rangle = \frac{l(2l-1)}{3} \int_{M_4+M_5} (\gamma_+ + \gamma_- - 2\gamma_0)\,dE \tag{A7}$$

where the $\gamma_{+,-,0}$ represent the absorption spectra with magnetic components $\nu = +1, -1$ and 0, respectively. Since, from (A6), the signal depends on $l_z^2$, one can measure both ferro(i)magnetic and antiferromagnetic ordering with linear dichroism.

The operators considered so far produce only *diagonal* matrix elements; that is, they do not mix the $\psi_{l,m}\,\chi_\sigma$ basis states, and can be written simply in terms of their occupation numbers, $\tfrac{6}{7}$ and $\tfrac{1}{7}$. The spin–orbit operator, on the other hand, *does* mix the basis states by

changing the quantum numbers $m$ and $\sigma$, so all four possible matrix elements contribute to $\langle l \cdot s \rangle$

$$\langle l \cdot s \rangle = \langle \psi | l_z s_z + \tfrac{1}{2} l_+ s_- + \tfrac{1}{2} l_- s_+ | \psi \rangle = -2 \tag{A8}$$

where the off-diagonal terms are generated by the ladder operators which act on the wavefunctions as

$$l_{\pm} \phi_{l,m} = [l(l+1) - m(m \pm 1)]^{1/2} \phi_{l,m\pm 1} \tag{A9}$$

and

$$s_{\pm} \chi_{\mp 1/2} = \chi_{\pm 1/2}. \tag{A10}$$

The non-zero off-diagonal terms are therefore all of the form

$$\langle \psi_{3,-3} \chi_{1/2} | l_- s_+ | \psi_{3,-2} \chi_{-1/2} \rangle = \langle \psi_{3,-2} \chi_{-1/2} | l_+ s_- | \psi_{3,-3} \chi_{1/2} \rangle = \sqrt{6} \tag{A11}$$

leading to a total off-diagonal contribution to the spin–orbit expectation value of 43%. In $LS$ coupling it is, of course, simpler to calculate $\langle l \cdot s \rangle$ directly from

$$\langle l \cdot s \rangle = \tfrac{1}{2} \left[ j(j+1) - l(l+1) - s(s+1) \right]. \tag{A12}$$

Finally, the magnetic dipole terms can be written

$$\langle T_z \rangle = \frac{3}{2(2l+3)(2l-1)} \langle \psi | (4q_{zz} s_z + l_z l_+ s_- + l_z l_- s_+ + l_+ s_- l_z + l_- s_+ l_z) | \psi \rangle = \frac{4}{7}. \tag{A13}$$

Interestingly, for this simple example, the diagonal contribution of

$$\frac{6}{(2l+3)(2l-1)} \langle \psi | q_{zz} s_z | \psi \rangle = \frac{2}{7} \tag{A14}$$

contributes exactly half of the total expectation value $\langle T_z \rangle$.

Equation (A13) shows that $\langle T_z \rangle$ provides a measure of the spin anisotropy when the charge distribution is distorted, either by spin–orbit interactions or by a crystal field, where the latter is weak for f metals. From (A14) we can interpret at least part of $\langle T_z \rangle$ as the spin-weighted quadrupole moment, which explains the strong correlation with charge anisotropy, magnetic anisotropy and, via (A7), linear dichroism. It is therefore of little surprise that although US has a cubic lattice (and therefore a zero crystal-field-induced quadrupole moment), it has a large magnetic anisotropy due to the strong 5f spin–orbit interaction, and a similarly strong $\langle T_z \rangle$.

While one could, in principle, deduce the moments for the configurations $f^2$, $f^3$, etc, in a similar way, many-electron wavefunctions must be antisymmetrized, which makes the calculations more tedious. To summarize, $\langle T_z \rangle$ can, under certain circumstances, be computed analytically. It is a sum over operator products, including $\langle l \cdot s \rangle$, or, alternatively, the quadrupole operator $q_{zz}$. Since strong spin–orbit coupling also tends to lead to strong magnetocrystalline anisotropy, one might expect highly anisotropic systems to exhibit large values of $\langle T_z \rangle$, and indeed, the present case of US is a good example of such a connection.

## References

[1] McWhan D B, Vettier C, Isaacs E D, Ice G E, Siddons D P, Hastings J B, Peters C and Vogt O 1990 *Phys. Rev.* B **42** 6007
[2] Gaulin B D, Gibbs D, Isaacs E D, Lussier J G, Reimers J N, Schröder A, Taillefer L and Zschack P 1994 *Phys. Rev. Lett.* **73** 890
[3] Isaacs E D, McWhan D B, Kleiman R N, Bishop D J, Ice G E, Zschack P, Gaulin B D, Mason T E, Garrett J D and Buyers W J L 1990 *Phys. Rev. Lett.* **65** 3185

[4]  Tang C C, Stirling W G, Lander G H, Gibbs D, Herzog W, Carra P, Thole B T, Mattenberger K and Vogt O 1992 *Phys. Rev.* B **46** 5287
[5]  Langridge S, Stirling W G, Lander G H and Rebizant J 1994 *Phys. Rev.* B **49** 12010
[6]  Hannon J P, Trammell G T, Blume M and Gibbs D 1988 *Phys. Rev. Lett.* **61** 1245; **62** 2644(E)
[7]  Jackson J D 1975 *Classical Electrodynamics* (New York: Wiley)
[8]  Lovesey S W 1993 *Rep. Prog. Phys.* **56** 257
[9]  Luo J, Trammell G T and Hannon J P 1993 *Phys. Rev. Lett.* **71** 287
[10] Carra P and Thole B T 1994 *Rev. Mod. Phys.* **66** 1509
[11] Lovesey S W and Collins S P 1996 *X-ray Scattering and Absorption by Magnetic Materials* (Clarendon: Oxford) at press
[12] van der Laan G, Thole B T, Sawatzky G A, Goedkoop J B, Fuggle J C, Esteva J M, Karnatak R, Remeika J P and Dabkowska H A 1986 *Phys. Rev.* B **34** 6529
[13] Gudat W and Kunz C 1972 *Phys. Rev. Lett.* **29** 169
[14] Winick H and Doniach S (ed) 1980 *Synchrotron Radiation Research* (New York: Plenum)
[15] Kitamura H 1992 *Synchrotron Radiat. News* **5** 114
[16] Elleaume P 1994 *J. Synchrotron Radiat.* **1** 19
[17] Giles C G, Malgrange C, Goulon J, DeBergevin F, Vettier C, Dartyge E, Fontain A, Giorgetti C and Pizzini S 1994 *J. Appl. Crystallogr.* **27** 232
[18] Brunel M, Patrat G, DeBergevin F, Rousseaux F and Lemonnier M 1983 *Acta Crystallogr.* A **39** 84
[19] Cooper M J, Laundy D, Cardwell D, Timms D N, Holt R and Clark G 1986 *Phys. Rev.* B **34** 5984
[20] Collins S P, Laundy D and Tang C C 1995 *Nucl. Instrum. Methods* B **97** 457
[21] Keski-Rahkonen O and Krause M O 1977 *Phys. Rev.* A **15** 959
[22] Storm E and Israel H I 1970 *At. Data Nucl. Data Tables* A **7** 565
[23] Kalkowski G, Kaindl G, Brewer W D and Krone W 1987 *Phys. Rev.* B **35** 2667
[24] Malgrange C, Carvalho C, Braichovich L and Goulon J 1991 *Nucl. Instrum. Methods* A **308** 390
[25] Ishikawa T 1989 *Rev. Sci. Instrum.* **60** 2058
[26] Finazzi M, Dias A M, Sainctavit Ph, Kappler J P, Krill G, Sanchez J P, Dalmas de Réotier P, Yaouanc A and Vogt O *Proc. Grand-Est Meeting (Strasbourg, 1995)*
[27] Fischer P, Schutz G, Stähler S and Wiesinger G 1991 *J. Appl. Phys.* **69** 6144
[28] Gibbs D, Harshman D R, Isaacs E D, McWhan D B, Mills D and Vettier C 1988 *Phys. Rev. Lett.* **61** 1241
[29] Tang C C, Stirling W G, Jones D L, Wilson C C, Haycock P W, Rollason A J, Thomas A H and Fort D 1992 *J. Magn. Magn. Mater.* **103** 86
[30] Gehring P M, Rebelsky L, Gibbs D and Shirane G 1992 *Phys. Rev.* B **45** 243
[31] Sanyal M K, Gibbs D, Bohr J and Wulff M 1994 *Phys. Rev.* B **49** 1079
[32] Thole B T, Carra P, Sette F and van der Laan G 1992 *Phys. Rev. Lett.* **68** 1943
[33] Carra P 1992 *Synchrotron Radiat. News* **5** 21
[34] Carra P, Thole B T, Altarelli M and Wang X 1993 *Phys. Rev. Lett.* **70** 694
[35] Schutz G, Knülle M and Ebert H 1993 *Phys. Scr.* T **49** 302
[36] Severin L, Brookes M S S, and Johansson B 1993 *Phys. Rev. Lett.* **71** 3214
[37] Cowan R D 1968 *J. Opt. Soc. Am.* **58** 808
[38] van der Laan G 1994 *J. Phys. Soc. Japan* **63** 2393
[39] Thole B T and van der Laan G 1994 *Phys. Rev.* B **49** 9613 section IV
[40] van der Laan G and Thole B T 1988 *Phys. Rev.* B **60** 1977
[41] Wedgewood F A 1972 *J. Phys. C: Solid State Phys.* **5** 2427
[42] Kobayashi K, Maruyama H, Iwazumi T, Kawamura N and Yamazaki H Solid State Commun. to be published
[43] Thole B T and van der Laan G 1993 *Phys. Rev. Lett.* **70** 2499